A Wing-Jet Interaction Theory for USB Configurations

C. Edward Lan*
University of Kansas, Lawrence, Kan.
and
James F. Campbell†
NASA Langley Research Center, Hampton, Va.

A linear, inviscid subsonic compressible flow theory is formulated to treat the aerodynamic interaction between the wing and an inviscid upper-surface blowing (USB) thick jet with Mach number nonuniformity. Because of Mach number nonuniformity, a two-vortex-sheet model for the jet surface is used to represent the induced flowfields inside and outside the jet. The induced flowfields and, therefore the wing aerodynamic characteristics due to the interaction, are computed by satisfying the wing tangency condition and the conditions of static pressure continuity and flow tangency on the jet surface. Application of the theory shows good agreement with available experimental data. It also is shown that conventional thin jet flap theories underestimate the lift for the USB configurations.

Nomenclature

A_j = jet cross-sectional area
b = span
c = local chord length
c_f = flap chord length
$\bar{c}$ = reference chord length
c_j = length of trailing jet to be included in the analysis
C = leading edge singularity parameter, see Eq. (43)
c_{di} = sectional induced drag coefficient
C_{Di} = induced drag coefficient
c_ℓ = sectional lift coefficient
$c_{\ell\Gamma}$ = sectional lift coefficient without jet reaction
C_L = total lift coefficient (circulation lift plus jet reaction lift)
$C_{L\Gamma}$ = circulation lift coefficient
C_m = pitching moment coefficient about the y axis
$C_{m\Gamma}$ = circulation pitching moment coefficient about the y axis
c_t = sectional leading-edge thrust coefficient
C_T = thrust coefficient of jet, thrust/$S_w q_0$
C_μ = jet momentum coefficient, $\dot{m}V_j/q_0 S_w$
$\boldsymbol{e}$ = unit vector tangent to jet path and surface
L = total lift
$\dot{m}$ = jet mass flow rate
M = Mach number, or number of integration points
$\boldsymbol{n}$ = unit vector normal to jet path and surface
$[N]$ = normal velocity influence coefficient matrix
N_1, N_2 = numbers of chordwise integration points on airfoil and flap, respectively
p = static pressure
q = dynamic pressure
R = radius of curvature
s = jet path coordinate
$[S]$ = tangential velocity influence coefficient matrix
S_w = wing area
T = ρ_o/ρ_j
t_j = jet thickness
u = nondimensional perturbed velocity in the x direction
$\boldsymbol{V}$ = unperturbed velocity vector
$\boldsymbol{v}$ = perturbed velocity vector
w = nondimensional perturbed velocity in the z direction
x,y,z = wing-fixed rectangular coordinates with positive x axis along the axis of symmetry pointing downstream, positive y axis pointing to the right, and positive z axis pointing upward
$z_c(x,y)$ = coordinate of camber surface
α = angle of attack, deg
β = $(1\text{-}M^2)^{1/2}$
δ_f = flap deflection, deg
δ_j = jet deflection angle, deg
η = static thrust recovery efficiency; ηC_T = actual thrust coefficient
γ = nondimensional vortex density, or ratio of specific heats
Λ = sweep angle, deg
μ = V_o/V_j
μ' = $\boldsymbol{V}_0 \cdot \boldsymbol{e}/\boldsymbol{V}_j \cdot \boldsymbol{e}$
ϕ = dimensional perturbation velocity potential, or angular coordinate
$\bar{\phi}$ = nondimensional perturbation velocity potential
ρ = density
ψ = nondimensional additional perturbation velocity potential
θ = angular coordinate
$\bar{\theta}(x)$ = angle of camber slope

Subscripts

1 = first endpoint of a vortex element
2 = second endpoint of a vortex element
a = additional
f = flap
j = jet flow
ℓ = leading edge
t = trailing edge
o = outer flow
w = wing
Γ = circulation
wo = perturbation due to wing in outer flow
wj = perturbation due to wing in jet flow
wa = additional wing vortices
oj = jet vortices for the outer flow
jj = jet vortices for the jet flow

Received July 21, 1975; revision received Jan. 13, 1976. This research was supported by NASA Grant NSG 1139 to the first author.
Index category: Aircraft Aerodynamics (including Component Aerodynamics).

*Associate Professor of Aerospace Engineering. Member AIAA.
†Head, Applied Aerodynamics Section, Subsonic-Transonic Aerodynamics Division. Associate Fellow AIAA.

Introduction

THE high lift capability of the upper-surface-blowing (USB) concept has been confirmed in early experiments by Turner, Davenport, and Riebe.[1] At that time, the high pressure-ratio jet was flattened to have less that 2% thickness relative to the local chord in order to simulate the turbojet engine exhaust. Recently, the USB concept has been under more extensive experimental investigation[2-10] than in the past. However, to simulate the modern or future high bypass-ratio turbofan engines, the low pressure-ratio jet in most of these experiments was relatively thick, being of the order of 10% of the local chord. Again, the promising aerodynamic and noise characteristics of the USB configurations have been confirmed.

Although the USB concept has been in existence for quite a while, only a few limited theoretical methods have been developed to describe the associated aerodynamic phenomena. In the inviscid theory, a possible theoretical method is the well-developed thin jet flap theory (see, for example, Ref. 11). However, experimental evidence[9] shows that the spreading of the USB jet flow is quite limited. With a narrow jet flow region of finite thickness on the wing and of higher dynamic pressure than the freestream, it is not unusual to expect that the thin jet flap theory is inadequate for the aerodynamic computation. In fact, for the similar type of configurations, Küchemann and Weber[12] have recognized for some time that additional lift would be induced on the lifting surface. This is because the wing induced flowfield would be modified by the jet region, and the jet flow also would be perturbed simultaneously, because of the presence of the wing. Since the thin jet flap theory does not account for this wing-jet interaction process, it is inadequate to describe the aerodynamic phenomena of the USB configuration. In fact, it has been shown numerically by Lan and Campbell[13] that the thin jet flap theory consistently underpredicted the USB lift.

Theoretically, in order to solve exactly the just mentioned wing-jet interaction problem, it would be necessary to solve the three-dimensional turbulent wall jet in the wing flowfield. Although the two-dimensional solution has been reported recently,[14] the three-dimensional problem appears formidable at the present time.

In this paper, the inviscid theory of wing-jet interaction, initially reported in Ref. 13, will be expounded further and applied to some USB configurations with different flap settings.

Method of Analysis

The main purpose of the present analysis is to determine numerically the wing aerodynamic characteristics in a freestream of Mach number M_o where there exists a high dynamic-pressure rectangular jet of finite thickness and of Mach number M_j on or above the wing surface. When the jet is on the wing surface, the configuration becomes that of the upper surface blowing. To simplify the analysis, it is assumed that 1) the unperturbed jet flow and freestream are uniform, and the perturbed flowfield in each region is governed by the Prandtl-Glauert equation with Mach number M_o or M_j, as the case may be; 2) the jet entrainment due to turbulent mixing is neglected; 3) the jet is of constant thickness and small deflection; and 4) the effects of fuselage, nacelle, and wing thickness are not included.

Boundary Conditions

The perturbation flowfields inside and outside the jet region are to be determined by satisfying the Prandtl-Glauert equations with M_o and M_j, subject to the following boundary conditions: that the jet surface be a stream surface and the static pressure be continuous across it, and that the flow be tangential to the wing surface. To satisfy the jet stream surface condition, it is required that the slopes of streamlines on both sides of the jet surface be the same. i.e.,

$$\frac{(n)\cdot(V_o+v_o)}{(e)\cdot(V_o+v_o)}=\frac{(n)\cdot(V_j+v_j)}{(e)\cdot(V_j+v_j)} \tag{1}$$

With the static pressure obtained from the Bernoulli equation, the pressure continuity condition becomes

$$p_j\left\{1+\frac{\gamma_j-1}{2}\frac{\rho_j}{\gamma_j p_j}\left[|V_j|^2-|V_j+v_j|^2\right]\right\}^{\gamma_j/(\gamma_j-1)}$$

$$=p_o\left\{1+\frac{\gamma_o-1}{2}\frac{\rho_o}{\gamma_o p_o}\left[|V_o|^2-|V_o+v_o|^2\right]\right\}^{\gamma_o/(\gamma_o-1)} \tag{2}$$

If it is assumed that, in the unperturbed flows, the static pressure is uniform throughout (i.e., $p_j=p_o$) and $\gamma_j=\gamma_o$, Eq. (2) can be simplified to be

$$\rho_j(V_j+v_j/2)\cdot v_j=\rho_o(V_o+v_o/2)\cdot v_o \tag{3}$$

To linearize Eqs. (1) and (3), let

$$v_j=(V_o\cdot n)n+\nabla\phi_j \tag{4}$$

$$v_o=\nabla\phi_o \tag{5}$$

where ϕ_o and ϕ_j are the perturbation velocity potentials. Substitution of Eqs. (4) and (5) into Eq. (1) gives, assuming $e\cdot(\nabla\phi_j)\ll e\cdot(V_j)$, $e\cdot(\nabla\phi_o)\ll e\cdot(V_o)$, and $V_j\cdot(n)=0$,

$$V_o\cdot n(1-\mu')+\partial\phi_o/\partial n\approx\mu'\partial\phi_j/\partial n \tag{6}$$

where

$$\mu'=V_o\cdot e/V_j\cdot e \tag{7}$$

Similarly, by retaining only the first-order terms, Eq. (3) can be reduced to

$$\rho_j(V_j\cdot e)\partial\phi_j/\partial s\approx\rho_o(V_o\cdot e)\partial\phi_o/\partial s \tag{8}$$

where $\partial\phi_j/\partial s=e\cdot\nabla\phi_j$, and s is the distance measured along the jet path and is taken to be x in the shallow jet assumption.

Since the wing is assumed to be completely in the outer flow, the conventional flow tangency condition is therefore applicable. It follows that the linearized wing surface boundary condition is given by

$$\partial\phi_o/\partial z=(V_o\cdot i)(\partial z_c/\partial x)-V_o\cdot k \tag{9}$$

where $z_c(x,y)$ is the wing camber function.

It is convenient to nondimensionalize these boundary conditions. For this purpose, the nondimensional perturbation potentials $\bar{\phi}_o$ and $\bar{\phi}_j$ are defined such that

$$\phi_o=(V_o\cdot e)\bar{\phi}_o,\quad \phi_j=(V_j\cdot e)\bar{\phi}_j \tag{10}$$

If it is assumed that $\partial(V_o\cdot e)/\partial n$ and $\partial(V_o\cdot e)/\partial s$ are small or zero, Eqs. (6), (8), and (9), become, respectively,

$$\frac{\partial\bar{\phi}_o}{\partial n}-\frac{\partial\bar{\phi}_j}{\partial n}=-\frac{V_o\cdot n(1-\mu')}{V_o\cdot e}\qquad\text{on jet surface} \tag{11}$$

$$\frac{\partial\bar{\phi}_j}{\partial s}-T(\mu')^2\frac{\partial\bar{\phi}_o}{\partial s}=o\qquad\text{on jet surface} \tag{12}$$

$$\frac{\partial\bar{\phi}_o}{\partial z}=\frac{V_o\cdot i}{V_o\cdot e}\frac{\partial z_j}{\partial x}-\frac{V_o\cdot k}{V_o\cdot e}\qquad\text{on wing surface} \tag{13}$$

where

$$T=\rho_o/\rho_j \tag{14}$$

Since the problem is linear, it can be decomposed into two subproblems, one being the wing-alone case with potential

$\bar{\phi}_w$ and the other being the interaction with additional potential ψ. However, because $M_j \neq M_o$, the decomposition should be done separately for the outer and the jet regions. Therefore, $\bar{\phi}_o$ and $\bar{\phi}_j$ can be written as

$$\bar{\phi}_o = \bar{\phi}_{wo}(M_o) + \psi_o(M_o) \tag{15}$$

$$\bar{\phi}_j = \bar{\phi}_{wj}(M_j) + \psi_j(M_j) \tag{16}$$

where $\bar{\phi}_{wo}$ and $\bar{\phi}_{wj}$ satisfy the Prandtl-Glauert equations with respective Mach numbers and the following boundary conditions

$$\frac{\partial \bar{\phi}_{wo}(M_o)}{\partial z} = \frac{\partial z_c}{\partial x} - \tan\alpha \tag{13a}$$

$$\frac{\partial \bar{\phi}_{wj}(M_j)}{\partial z} = \frac{\partial z_c}{\partial x} - \tan\alpha \tag{13b}$$

where the right-hand side of both equations is the same as that of Eq. (13).

Substitution of Eqs. (15) and (16) into Eqs. (11-13) gives

$$\frac{\partial \psi_o}{\partial n} - \frac{\partial \psi_j}{\partial n} = -\frac{V_o \cdot n(1-\mu')}{V_o \cdot e} + \frac{\partial \bar{\phi}_{wj}(M_j)}{\partial n} - \frac{\partial \bar{\phi}_{wo}(M_o)}{\partial n} \tag{17}$$

$$\frac{\partial \psi_j}{\partial s} - T(\mu')^2 \frac{\partial \psi_o}{\partial s} = -\frac{\partial \bar{\phi}_{wj}}{\partial s} + T(\mu')^2 \frac{\partial \bar{\phi}_{wo}}{\partial s} \tag{18}$$

$$\frac{\partial \psi_o}{\partial z} = 0 \tag{19}$$

It is seen easily that if there is no jet (i.e., $\mu' = 1$, $M_o = M_j$, and $T = 1$), Eqs. (17-19) automatically will produce zero additional perturbation potentials ψ_o and ψ_j. Equations (17) and (18) imply discontinuity in the normal and tangential perturbed velocities on the jet surface. In the foregoing, the jet boundary conditions are satisfied on the undeformed jet surface; whereas the mean surface approximation is used for satisfying the wing boundary condition.

Method of Flow Singularity

From Eqs. (15) and (16), it is seen that ψ_o and ψ_j also satisfy the Prandtl-Glauert equation. It is well known that a vortex is a fundamental solution of the Prandtl-Glauert equation. Therefore, it is appropriate to use vortex distributions to represent the wing and the jet surface. However, because of Mach number nonuniformity, a vortex distribution on the jet surface would induce different normal and tangential velocities at all other points on the jet surface depending on whether the surface is approached from inside or outside the jet region. Therefore, it can not satisfy both Eqs. (17) and (18) simultaneously. It is possible to introduce a source distribution to account for the jump in the normal velocity. However, such a source distribution would be dependent on the vortex distribution introduced to satisfy Eq. (18) and vice versa, again, because of Mach number nonuniformity. Besides, additional new integrals for the source distribution must be handled. Therefore, it is most convenient for the present problem to introduce two vortex sheets on the jet surface, with one sheet to account for the perturbations in the outer flow and the other for the jet flow. The strengths of the vortex sheets are determined by satisfying Eqs. (17-19). This vortex model is illustrated in Fig. 1. The wing is seen to be influenced by the outer jet vortices in the form of additional upwash, whereas the jet region is affected only by the inner jet vortices.

With vortex sheets introduced in the flowfield, the induced normal and tangential velocities along the boundary must be evaluated in terms of the unknown vortex strengths. In the present method, these vortex integrals are reduced to finite sums through the quasi-vortex-lattice method (quasi VLM).[15] The boundary conditions are satisfied exactly only at a discrete number of points (i.e., control points). The vortex strengths are computed at an equal number of locations (i.e., vortex locations). The control points and vortex locations are based on the "semicircle method" and are chosen to account for the square root singularities and the Cauchy singularity. The results can be formulated in the format of influence coefficient matrices. Define $[S_{JW}]$ as the s-influence coefficient matrix for the jet region because of the wing; i.e., the matrix elements being the tangential perturbed velocities on the jet surface because of unit vortex elements on the wing. Similar definitions are applicable to the matrices $[N_{JW}]$, $[N_{WW}]$, $[N_{WJ}]$, etc., where N denotes the normal components. Using γ with appropriate subscripts to denote the unknown vortex strength, the additional perturbed velocities at the control points on the jet surface can be written as

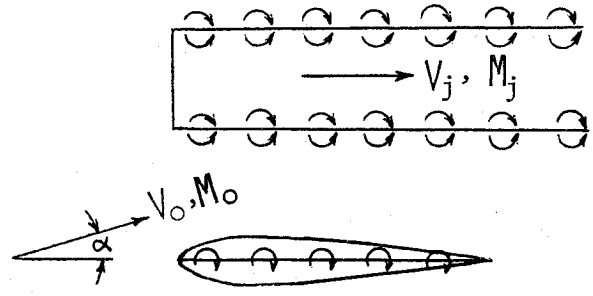

Fig. 1 Illustration of the vortex model for wing-jet interaction.

$$\{\partial \psi_o/\partial n\} = [N_{JW(o)}]\{\gamma_{wa}\} + [N_{JJ(o)}]\{\gamma_{oj}\} \tag{20}$$

$$\{\partial \psi_j/\partial s\} = [N_{JJ(j)}]\{\gamma_{jj}\} \tag{21}$$

$$\{\partial \psi_o/\partial s\} = [S_{JW(o)}]\{\gamma_{wa}\} + [S_{JJ(o)}]\{\gamma_{oj}\} \tag{22}$$

$$\{\partial \psi_j/\partial s\} = [S_{JJ(j)}]\{\gamma_{jj}\} \tag{23}$$

where the subscripts "o" and "j" denote the outer and the jet regions, respectively. $\{\gamma_{wa}\}$ are the additional wing vortex strengths induced by the jet. Similarly, the induced normal velocities at the wing control points can be written as

$$\{\partial \psi_o/\partial z\} = [N_{ww}]\{\gamma_{wa}\} + [N_{WJ(o)}]\{\gamma_{oj}\} \tag{24}$$

When Eqs. (20-24) are substituted into Eqs. (17-19), a set of coupled matrix equations is obtained. Writing them in the format of an augmented matrix equation, they can be solved for the unknown discrete vortex densities by Purcell's vector method.[16] The main advantage of this solution technique is that it requires only $(N_m+1)^2/4$ memory locations for the matrix operation, where N_m is the matrix size.

Once the additional wing vortex strengths γ_{wa} have been determined, the total wing γ_w is then

$$\gamma_w = \gamma_{wo} + \gamma_{wa} \tag{25}$$

where γ_{wo} is the wing vortex strength in the jet-off case.

It should be noted that the discrete-element approximation, formulated so far, can not give accurate induced tangential velocities, or $[S]$ matrices. To illustrate, consider the expression for $u(x,z)$ for the two-dimensional case in incompressible flow:

$$u(x,z) = \frac{z}{2\pi}\int_o^l \frac{\gamma(x')\,dx'}{(x-x')^2+z^2} \tag{26}$$

At $z=0$, the discrete-element approximation would give zero for $u(x,o)$, instead of the correct value $\gamma(x)/2$. In the present

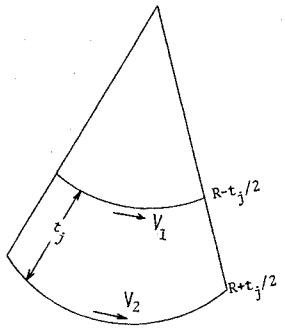

Fig. 2 Geometry of a jet cross section.

method, $u(x,o)$ is assigned a value equal to $\gamma(x)/2$ without computation. When z is small but not zero, Eq. (26) is rewritten as

$$u(x,z)=\frac{z}{2\pi}\int_o^l \frac{\gamma(x')-\gamma(x)}{(x-x')^2+z^2}\,dx'+\frac{z\gamma(x)}{2\pi}\int_o^l \frac{dx'}{(x-x')^2+z^2}$$

$$\cong \frac{z}{4\pi}\frac{\pi}{N}\sum_{k=1}^{N}\frac{\gamma(\theta_k)-\gamma(x)}{(x-x_k)^2+z^2}\sin\theta_k$$

$$+\frac{z\gamma(x)}{4\pi}\frac{\pi}{M}\sum_{j=1}^{M}\frac{\sin\theta_j}{(x-x_j)^2+z^2} \tag{27}$$

where

$$\theta_k=(2k-1)\pi/2N,\ x_k=(1-\cos\theta_k)/2,\ k=1,\ldots,N \tag{28}$$

$$\theta_j=(2j-1)\pi/2M,\ x_j=(1-\cos\theta_j)/2,\ j=1,\ldots,M \tag{29}$$

and M is chosen so that

$$M=2^pN \tag{30}$$

for interdigitation between the control and integration points in the last summation and p is an arbitrary integer greater than 1. This method of integration has been shown [17] to be quite accurate if $p\geq 3$.

The detail expressions for the influence coefficient matrices can be obtained easily by use of the general vector form of induced velocities due to a vortex element, given in Ref. 15. For convenience, they are listed in the Appendix.

Jet Flap Effect

Because of the Coanda effect, the jet sheet tends to follow the wing upper surface and leaves the trailing edge at a given angle. Behind the trailing edge, the curvature of the jet sheet changes continuously, very much like that in the thin jet flap theory.[18] Since the curvature distribution is unknown and is dependent on the unknown jet vortex strength, the term $\boldsymbol{V}_o\cdot\boldsymbol{n}$ in Eq. (17) also would be unknown. To avoid iteration, Spence's method in the thin jet flap theory[18] is adapted in the following way for the present thick jet applications. As shown in Fig. 2, irrotationality of the jet flow implies that

$$V_1(R-t_j/2)=V_2(R+t_j/2) \tag{31a}$$

or,

$$V_1-V_2=V_jt_j/R \tag{31b}$$

where $V_j=(V_1+V_2)/2$. Note that both V_1 and V_2 are dimensional total jet velocities. In terms of nondimensional perturbed potential [Eq. (10)] they can be expressed as

$$V_1=V_j+V_j(\partial\bar{\phi}_j/\partial s)_1 \tag{32a}$$

$$V_2=V_j+V_j(\partial\bar{\phi}_j/\partial s)_2 \tag{32b}$$

It follows from Eq. (31) that

$$\frac{t_j}{R}=\left(\frac{\partial\bar{\phi}_j}{\partial s}\right)_1-\left(\frac{\partial\bar{\phi}_j}{\partial s}\right)_2$$

$$=T(\mu')^2\left[\left(\frac{\partial\bar{\phi}_o}{\partial s}\right)_1-\left(\frac{\partial\bar{\phi}_o}{\partial s}\right)_2\right] \tag{33}$$

where Eq. (12) has been used. Equation (33) is consistent with Spence's results in that, for a thin jet, if $(\partial\bar{\phi}_0/\partial s)_1-(\partial\bar{\phi}_o/\partial s)_2=\gamma_j$, the jet vortex strength would be $\bar{\gamma}_j=t_j\rho_\pi V_j^2/\rho_o V_o^2R$. This agrees with Eq. (26) of Ref. 18. Using Eq. (15), Eq. (33) can further be written as

$$\frac{t_j}{R}=T(\mu')^2\left[\left(\frac{\partial\psi_o}{\partial s}\right)_1-\left(\frac{\partial\psi_o}{\partial s}\right)_2\right.$$

$$\left.+\left(\frac{\partial\bar{\phi}_{wo}}{\partial s}\right)_1-\left(\frac{\partial\bar{\phi}_{wo}}{\partial s}\right)_2\right]=f(x,y) \tag{34}$$

Assuming shallow jet approximation, $1/R\cong d^2z/dx^2$. It follows that the jet path satisfies the following initial value problem:

$$t_j(d^2z/dx^2)=f(x,y) \tag{35a}$$

$$z(t.e.)=0 \tag{35b}$$

$$(dz/dx)(t.e.)=-\delta_j \tag{35c}$$

Since only the slope dz/dx is needed at a given spanwise station, only the second initial condition is required for integration. Although the trailing jet is of infinite extent downstream, only a finite length c_j is needed for numerical convergence. To integrate Eq. (35), let

$$x=x_t+c_j(1-\cos\theta)/2 \tag{36}$$

Eq. (35) becomes

$$t_j(d/d\theta)(dz/dx)=(c_j/2)\sin\theta f(\theta,y)$$

which can be integrated once to give the slope at control point i

$$t_j\left(\frac{dz}{dx}\right)_i=-t_j\delta_j+\int_o^{\theta_i}\frac{c_j}{2}\sin\theta f(\theta,y)\,d\theta$$

$$\cong -t_j\delta_j+\frac{(\Delta\theta)c_j}{2}\left[\sum_{k=1}^{i-1}\sin\theta_k f(\theta_k,y)+\tfrac{1}{2}\sin\theta_i f(\theta_i,y)\right] \tag{37}$$

where the integral has been reduced to a finite sum through the trapezoidal rule. This method of integration has been found to be more efficient than the point-slope formula. With dz/dx obtained from Eq. (37), $\boldsymbol{V}_o\cdot\boldsymbol{n}/\boldsymbol{V}_o\cdot\boldsymbol{e}$ in Eq. (17) can be written as

$$\boldsymbol{V}_o\cdot\boldsymbol{n}/\boldsymbol{V}_o\cdot\boldsymbol{e}=-dz/dx+\tan\alpha \tag{38}$$

The slope dz/dx involves the unknown vortex strength through the function $f(\theta,y)$ [Eqs. (37) and (34)]. These terms can be combined with the left-hand side of Eq. (17) before the solution is attempted.

Aerodynamic Forces and Moments

The sectional characteristics can be computed by properly resolving the pressure force, which acts normal to the camber surface, into appropriate directions. It follows that

$$c_\ell=\frac{2}{\rho_oV_o^2c}\int_{x_\ell}^{x_t}\rho_oV_o(\boldsymbol{V}_o\cdot\boldsymbol{e})\gamma_w(x)\cos(\alpha-\bar{\theta}(x))\,dx$$

$$+c_t\sin(\alpha-\bar{\theta}_{t'})=\frac{2\cos\alpha}{c}\int_{x_{t'}}^{x_t}\gamma_w(x)\cos(\alpha-\bar{\theta}(x))\,dx$$

$$+c_t\sin(\alpha-\bar{\theta}_{t'}) \tag{39}$$

$$c_{di}=\frac{2\cos\alpha}{c}\int_{x_{t'}}^{x_t}\gamma_w(x)\sin(\alpha-\bar{\theta}(x))\,dx-c_t\cos(\alpha-\bar{\theta}_{t'}) \tag{40}$$

$$c_m=\frac{2\cos\alpha}{\bar{c}c}\int_{x_{t'}}^{x_t}\gamma_w(x)x\cos(\alpha-\bar{\theta}(x))\,dx \tag{41}$$

where

$$\bar{\theta}(x)=\tan^{-1}(dz_c/dx) \tag{42}$$

The sectional leading-edge thrust coefficient c_t is computed as[15]

$$c_t=(\pi/2\cos\Lambda_{t'})\,(1-M_o^2\cos^2\Lambda_{t'})^{1/2}C^2 \tag{43}$$

where C is the leading-edge singularity parameter. According to the quasi VLM,[15] the parameter C can be determined by summing the total induced normal velocity at the leading edge and subtracting the right-hand side of Eq. (17) or (19), depending on whether the effects of wing alone or the jet interaction are being considered. If the induced normal velocity at the ith leading edge control point is denoted by a subscript i, then the singularity parameter C_1 in the wing-alone case with flap deflection can be computed from the expression[15]

$$N_1C_1[(x_f-x_{t'})/c]^{-1/2}(\tan^2\Lambda_{t'}+\beta^2)^{1/2}$$

$$=[N_{ww}]_i\{\gamma_{wo}\}-\{\partial z_c/\partial x-\tan\alpha\}_i \tag{44}$$

Similarly, for the additional perturbation, it can be shown from Eqs. (19) and (24) that

$$N_1C_2[(x_f-x_{t'})/c]^{-1/2}(\tan^2\Lambda_{t'}+\beta^2)^{1/2}$$

$$[N_{ww}]_i\{\gamma_{wa}\}+[N_{WJ(o)}]_i\{\gamma_{oj}\} \tag{45}$$

The singularity parameter for the combined problem then is $C=C_1+C_2$.

The integration in Eqs. (39-41) is evaluated first by transforming the interval to an angular coordinate θ:

$$x=(x_f-x_{t'})\,(1-\cos\theta)/2+x_{t'} \tag{46}$$

for the airfoil, and

$$x=x_f+(x_t-x_f)\,(1-\cos\theta)/2 \tag{47}$$

for the flap. The results then are reduced to finite sums through the midpoint trapezoidal rule. For example, the sectional lift coefficient can be computed as

$$c_{t'}=\frac{2\cos\alpha}{c}\left(\int_{x_{t'}}^{x_f}+\int_{x_f}^{x_t}\right)\gamma_w(x)\cos(\alpha-\bar{\theta}(x))\,dx+c_t\sin(\alpha-\bar{\theta}_{t'})$$

$$\cong\frac{2\cos\alpha}{c}\left[\frac{x_f-x_{t'}}{2}\frac{\pi}{N_1}\sum_{k=1}^{N_1}\gamma_w(x_k)\cos(\alpha-\bar{\theta}(x_k))\sin\theta_k\right.$$

$$\left.+\frac{x_t-x_f}{2}\frac{\pi}{N_2}\sum_{k=1}^{N_2}\gamma_w(x_k)\cos(\alpha-\bar{\theta}(x_k))\sin\theta_k\right]$$

$$+c_t\sin(\alpha-\bar{\theta}_{t'}) \tag{48}$$

where $\theta_k=(2k-1)\pi/2N_1$, $k=1,\ldots,N$, and $(2k-1)\pi/2N_2$, $k=1,\ldots,N_2$ on the airfoil and the flap, respectively. Similar formulas can be derived for c_{di} and c_m.

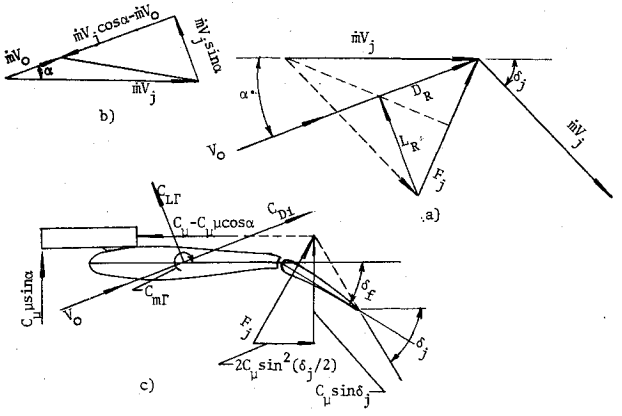

Fig. 3 Force systems acting on a USB configuration.

The overall aerodynamic characteristics of the wing are determined by spanwise integration of the sectional characteristics. Again, the integration first is transformed to an angular coordinate $\phi(0\le\phi\le\pi)$ and then is reduced to finite sums through the midpoint trapezoidal rule. For example, if the jet span extends from b_1 to b_2, the wing lift coefficient can be computed as

$$C_L=\frac{1}{S_w}\int_{-b/2}^{b/2}c_t c\,dy=\frac{2}{S_w}\left\{\int_o^{b_1}c_t c\,dy+\int_{b_1}^{b_2}c_t c\,dy+\int_{b_2}^{b/2}c_t c\,dy\right\}$$

$$\cong\frac{2}{S_w}\left\{\frac{b_1}{2}\frac{\pi}{M_1}\sum_{i=1}^{M_1-1}c_{t'i}c_i\sin\phi_i\right.$$

$$+\frac{b_2-b_1}{2}\frac{\pi}{M_2}\sum_{i=1}^{M_2-1}c_{t'i}c_i\sin\phi_i$$

$$\left.+\frac{b/2-b_2}{2}\frac{\pi}{M_3}\sum_{i=1}^{M_3-1}c_{t'i}c_i\sin\phi_i\right\} \tag{49}$$

where $\phi_i=i\pi/M_1$, $i\pi/M_2$, and $i\pi/M_3$, respectively, for the three intervals.

Coanda Effects

It is well known that the jet on the wing upper surface tends to stay on the surface, even if the flap is deflected. This is because, with the flap deflected, the jet entrainment caused by turbulent mixing would create suction pressure between the jet and the flap surface, resulting in the jet being attracted toward the flap surface. This Coanda effect exists also under wind-off conditions. Since this effect can be explained only by the viscous flow theory, its exact prediction is out of the scope of the present investigation. For the present purpose, the forces and moment associated with the Coanda effect will be computed in accordance with the linear momentum principle. As illustrated in Fig. 3a, when the jet is deflected at the flap hinge, a jet reaction F_j equal to $2\dot{m}V_j\sin(\delta_j/2)$ will be produced on one side of the wing. Its lift and drag components are therefore

$$L_R=2\dot{m}V_j\sin(\delta_j/2)\cos(\delta_j/2+\alpha) \tag{50}$$

$$D_R=2\dot{m}V_j\sin(\delta_j/2)\sin(\delta_j/2+\alpha) \tag{51}$$

Furthermore, when the nacelle inlet is at an angle of attack, a force would also be developed. According to Fig. 3b, this force has the following lift and drag components:

$$L_\alpha=\dot{m}V_j\sin\alpha \tag{52}$$

$$D_\alpha=-(\dot{m}V_j\cos\alpha-\dot{m}V_o) \tag{53}$$

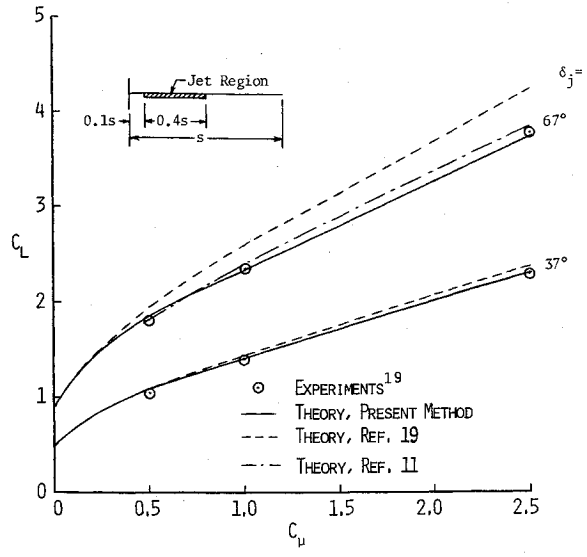

Fig. 4 Comparison of predicted lift coefficient for a rectangular wing due to partial span flap and blowing trailing-edge jet by thin jet flap theories and experiments ($AR=6$, $c_f/c=0.1$, and $\alpha=0°$).

The sum of Eqs. (50) and (52) gives the total lift due to the operation of the jet engines:

$$L_j=2\dot{m}V_j\sin(\delta_j/2)\cos(\delta_j/2+\alpha)+\dot{m}V_j\sin\alpha$$

$$=\dot{m}V_j\sin(\delta_j+\alpha) \tag{54}$$

Similarly, the drag component is

$$D_j=2\dot{m}V_j\sin(\delta_j/2)\sin(\delta_j/2+\alpha)-\dot{m}V_j\cos\alpha+\dot{m}V_o$$

$$=\dot{m}V_j[V_o/V_j-\cos(\delta_j+\alpha)] \tag{55}$$

The aforementioned forces, acting on the wing and nacelles, also would produce the pitching moment, the calculation of which is straightforward. These nonaerodynamic forces are depicted in Fig. 3c. Note that the jet reaction F_j does not act necessarily through the flap hinge, because δ_j, in general, is not the same as δ_f because of the airfoil surface curvature.

Numerical Results and Discussions

Some early results of the present method have been reported in Ref. 13. Since then, the computer program has been generalized to accommodate more general configurations, and the tangential velocity computation has been refined further. The improved program now can treat the thick jet applications or the thin jet flap theory at the user's choice.

Since there are no other USB theoretical results available for comparison, it is appropriate to compare the present thin jet flap computation with other thin jet theories. According to the thin jet flap concept, it is assumed that $V_j/V_o\to\infty$, but $V_j^2t_j$ is finite, where t_j is the jet thickness. It follows that $\mu'=0$ and $\partial\bar{\phi}_j/\partial n=0$ in Eq. (11). Furthermore, the expression $T(\mu')^2/t_j$ appearing in Eq. (34) can be simplified as

$$\frac{T(\mu')^2}{t_j}=\frac{\rho_oV_o^2}{\rho_jV_j^2t_j}=\frac{2}{c_\mu c} \tag{56}$$

where c_μ is the sectional jet momentum coefficient. In the present method, the jet thickness is assumed to be 5% of the local chord. The trailing jet length, c_j in Eq. (36), to be included in the analysis, was determined numerically by varying c_j for a given number of streamwise vortices until a maximum value for $C_{L\Gamma}$ was predicted. From this numerical experimentation, it was found that, for practical purposes, a c_j equal to 2 local chord lengths and 6 streamwise vortices per strip is sufficient for numerical convergence. The results for a rectangular wing with a partial span flap are compared in Fig. 4 with those given in Fig. 9 of Ref. 19. The theoretical results given by Lopez and Shen[11] are also shown for $\rho_j=67°$. It is seen that C_L, predicted by the present method, is in good agreement with other theoretical predictions and experiments.

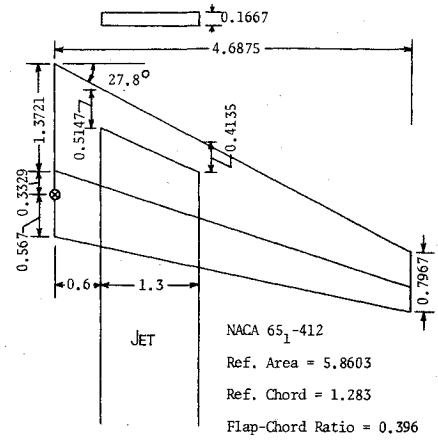

Fig. 5 Idealized USB configuration of Ref. 2 (the center of gravity is 0.489 below the wing plane).

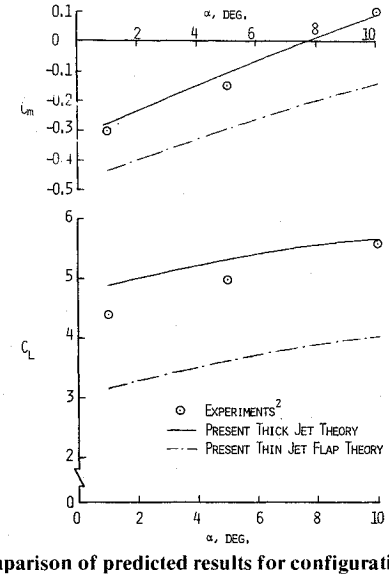

Fig. 6 Comparison of predicted results for configuration of Fig. 5 by thick jet theory and thin jet flap theory with experiments ($C_T=2.095$, $\eta=80\%$, $M_o=M_j=0$, $\delta_f=\delta_j=46.7°$, and $\mu=0.19289$).

In comparing the theory with some available USB experimental data, it should be noted that the data usually do not show the actual jet velocity, and the engine thrust was calibrated by the fan rotational speed with wind off and with deflectors and/or flap removed. For simplicity, it is assumed in the computation that the jet velocity is calculated by applying the momentum theory,

$$\frac{V_j}{V_o}=\tfrac{1}{2}\left(1+\left[1+\frac{2C_T(S_w/2)}{A_j(\rho_j/\rho_o)}\right]^{1/2}\right) \tag{57}$$

where A_j is the jet cross-sectional area, and C_T is the total thrust coefficient, subject to the modification by the static thrust recovery efficiency η, as was done in Ref. 5.

The first test configuration given in Ref. 2 is idealized in Fig. 5. The idealized full-span flap includes the flap extension which is attached to and deflected 16.7° relative to a simple flap system. The area of flap extension is not included in the reference area, except that a small area extended from the original root chord of the flap extension to the centerline of

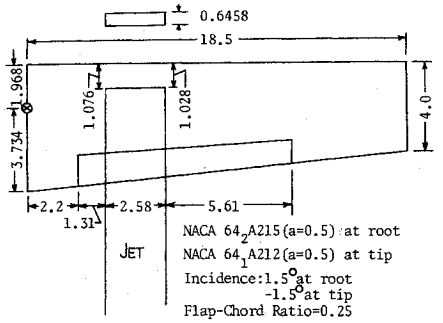

Fig. 7 Idealized USB configuration of Ref. 5 (the center of gravity is 3.5 below the wing plane).

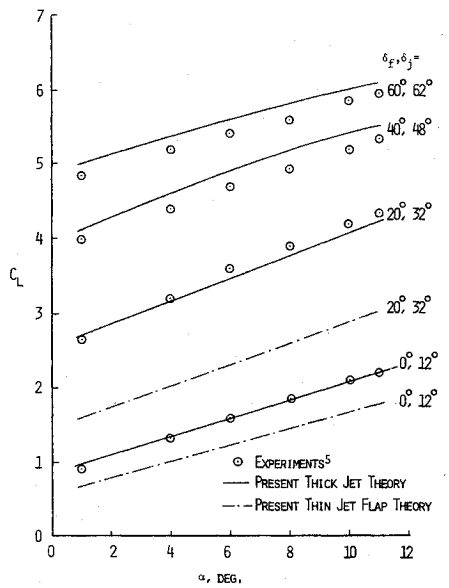

Fig. 8 Comparison of predicted lift coefficient for configuration of Fig. 7 by thick jet theory and thin jet flap theory with experiments ($C_T = 2$, $\eta = 100\%$, $M_o = M_j = 0$, and $\mu = 0.1288$).

the model. Because of the use of a deflector, the static thrust recovery efficiency was found in Ref. 2 to be only 80%. No attempt was made to account for the leading-edge Krueger flap, nacelle, and the fuselage. Therefore, it is appropriate to determine the total aerodynamic characteristics by adding the prediced incremental values due to the jet interaction to the experimental wing-alone data. From numerical experimentation, the length of trailing jet c_j used in the analysis was determined to be one local chord length with 5 streamwise vortices per strip, to produce practically maximum $C_{L\Gamma}$ within reasonable computing time. This is used in all of the following computations. The results are plotted in Fig. 6. For simplicity, the flap angle is assumed to be the same as the jet deflection angle, which is 46.7° in the aerodynamic computation. The results indicate that the thin jet flap theory largely underestimates the lift and predicts higher negative pitching moment. In computing the pitching moment by the thin jet flap theory, the jet reaction is assumed to be acting at the trailing edge. The present thick jet theory slightly overpredicts the lift. It should be noted that the skin friction and jet scrubbing drag are not included in the pitching moment computation.

To test the theory further, the experimental data of Ref. 5 are chosen for comparison. The configuration is shown in Fig. 7. Note that at a given flap angle, the jet tends to follow the airfoil upper surface curvature and deflects at a higher angle at the trailing edge. According to Ref. 5, this additional angle is 12°. However, at high flap angles, the jet failed to

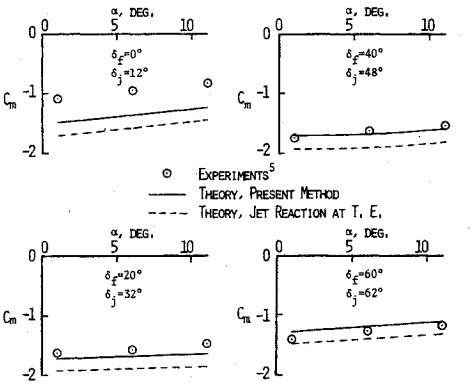

Fig. 9 Comparison of predicted pitching moment coefficient for configuration of Fig. 7 by thick jet theory with experiments ($C_T = 2$, $\eta = 100\%$, $M_o = M_j = 0$, and $\mu = 0.1288$).

follow the surface. In order to compare realistically with the experimental data, the jet deflection angle is taken to be the experimental value measured under wind-off conditions. Because of relatively low freestream test velocity, the Mach numbers are assumed to be zero. The lift data are compared in Fig. 8. The thick jet theory gives reasonably good agreement at low flap angles; whereas, again, the thin jet flap theory underpredicts the lift. The pitching moment data are given in Fig. 9. In computing the pitching moment, it is important to account accurately for all nonaerodynamic forces. In the present configuration, the Fowler flap system not only deflects but also extends, to make the determination of the moment arm for the Coanda force difficult. The present results are computed by measuring this moment arm directly from Fig. 3 of Ref. 5. Again, the skin friction and the scrubbing drag which would produce more positive moment are not included. If the jet reaction is assumed to be at the trailing edge, the results are shown as the dashed lines. It appears that assuming the jet reaction at the trailing edge tends to produce more negative moment.

Direct comparison of the induced drag computation is difficult because the experimental data are not available. However, if it is assumed that the skin friction and the jet scrubbing drag are approximately independent of the angle of attack, then the quantity

$$\Delta C_{D\alpha} = (C_{Di} + C_{Dj})_{(\alpha)} - (C_{Di} + C_{Dj})_{(\alpha = l^\circ)} \tag{58}$$

represents the incremental induced drag due to the angle of attack. The results for the configuration of Fig. 5 are shown in Table 1 and those for Fig. 7 in Table 2. The results are in reasonably good agreement with the experimental data.

Having established the accuracy for the present method, it is of interest to see how the Mach number nonuniformity will affect the loading. Since no controlled experiments are available for comparison, only theoretical results will be shown. For this purpose, it is assumed that, for the configuration of Fig. 7, $M_o = 0.1$ and $\mu = 0.1288$ are fixed. The jet

Table 1 Comparison of predicted induced drag increments due to angle of attack for configuration of Fig. 5 with experiments (Ref. 2)[a]

	$\Delta C_{D(\alpha)}$	
α°	Theory	Experiment
5	0.277	0.3
10	0.619	0.65

[a] $C_T = 2$, $\eta = 100\%$, $M_o = M_j = 0$. $\delta_f = 46.7°$, $\delta_j = 46.7°$.

Table 2 Comparison of predicted induced drag increments due to angle of attack for configuration of Fig. 7 with experiments (Ref. 5)[a]

δ_f°	0		20		40		60	
	$\Delta C_{D(\alpha)}$		$\Delta C_{D(\alpha)}$		$\Delta C_{D(\alpha)}$		$\Delta C_{D(\alpha)}$	
α°	Theory	Experiment	Theory	Experiment	Theory	Experiment	Theory	Experiment
6	0.096	0.15	0.233	0.2	0.322	0.3	0.375	0.35
11	0.227	0.3	0.5	0.5	0.658	0.6	0.752	0.65

[a] $C_t = 2, \eta = 100\%, M_o = M_j = 0$.

Mach numbers then are computed according to the following relation:

$$M_j = (M_o/\mu)(\rho_j/\rho_o)^{1/2} \tag{59}$$

Figure 10 shows the results for spanwise distribution of induced drag and circulation lift coefficients. It is seen that higher M_j induces higher loading and induced drag; whereas higher jet temperature (lower density) produces lower loading. It should be noted that, in reality, the loading probably will not be as concentrated as shown in Fig. 10 because of jet spreading. The peaks in the loading and the induced drag distributions probably are because of the effect of jet side surfaces. This can be explained qualitatively as follows. As has been shown before,[20] the jet interaction can be explained by reflection and diffraction of disturbances. The reflection causes increase in lift whereas the diffraction decreases it. Assume the jet extent is infinite in the streamwise direction. Consider an originating vortex "*a*" near the side surface (see Fig. 11). The disturbance created by it will be reflected back at the jet lower surface and diffracted into the jet region. The latter can be represented by the vortex "*b*." This diffracted disturbance will be reflected not only at the jet upper surface, but also at the side surface. The latter is represented by the vortex "*c*." It is seen that the vortex"*c*" tends to diminish the effect of "*b*," which eventually will be diffracted back to the region of the originating vortex to decrease the lift. Because of the decrease in strength of the final diffracted diturbance, the lift is increased. Near the center of the jet span, the side surface effect is small, so that the situation will be closer to the two-dimensional case.[20] This three-dimensional "spreading effect" also has been noted in Ref. 17.

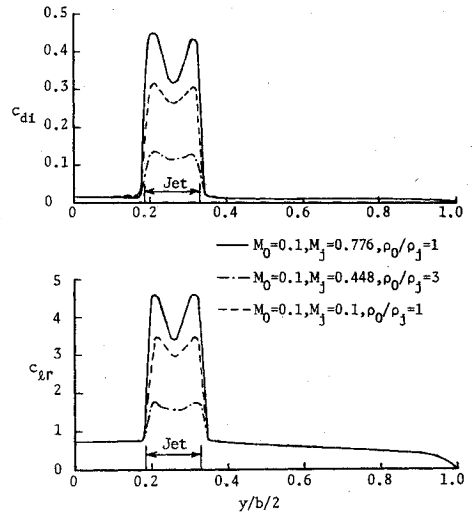

Fig. 10 Effects of mach number nonuniformity and jet density on aerodynamic characteristics ($\alpha = 5°$, $\delta_f = 0°$ and $\mu = 0.1288$).

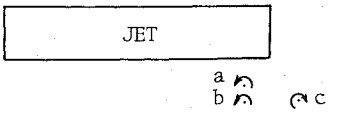

Fig. 11 Schematic illustration of effects of jet side surfaces by image vortices.

Conclusions

A theoretical method has been formulated which accounts for the wing-jet interaction with Mach number nonuniformity for the USB configurations. Comparison of the predicted results with experimental data showed good agreement in lift, induced drag, and pitching moment. It also was shown that the thin jet flap theory is inadequate for the USB configurations with thick jet.

Appendix: Expressions for Influence Coefficient Matrices

For the purpose of satisfying the boundary conditions, the continuous vortex distributions are assumed to be stepwise constant in the spanwise direction and continuous in the streamwise direction. Therefore, the wing and the jet surfaces now are covered with vortex strips, in which there are bounded and trailing elements. The induced velocity vector $\boldsymbol{v}_l$ at a control point i because of the bounded vortex of one strip is given by[15]

$$\boldsymbol{v}_l(\boldsymbol{R}_i) = \frac{\beta^2}{4\pi}\left(\int_{x_l}^{x_f} + \int_{x_f}^{x_l}\right)\gamma(\xi)\boldsymbol{M}(\xi,\boldsymbol{R}_i)\,d\xi$$

$$\cong \frac{\beta^2}{4\pi}\left[\frac{x_f - x_l}{2}\frac{\pi}{N_l}\sum_{k=1}^{N_l}\gamma(\theta_k)\boldsymbol{M}(\Theta_k,\boldsymbol{R}_i)\sin\theta_k + \frac{x_l - x_f}{2}\frac{\pi}{N_2}\sum_{k=1}^{N_2}\gamma(\theta_k)\boldsymbol{M}(\theta_k,\boldsymbol{R}_i)\sin\theta_k\right] \tag{A1}$$

where

$$\boldsymbol{R}_i = x_i\boldsymbol{i} + y_i\boldsymbol{j} + Z_i\boldsymbol{k} \tag{A2}$$

$$\xi_k = x_l + (x_f - x_l)(1 - \cos\theta_k)/2,$$

$$\theta_k = (2k-1)\pi/2N_l, k = 1,\ldots,N_l \tag{A3}$$

$$x_i = x_l + (x_f - x_l)(1 - \cos\theta_i)/2,$$

$$\theta_i = i\pi/N_l,\ i = 1,\ldots,N_l \tag{A4}$$

on the airfoil, and

$$\xi_k = x_f + (x_l - x_f)(1 - \cos\theta_k)/2,$$

$$\theta_k = (2k-1)\pi/2N_2,\ k = 1,\ldots,N_2 \tag{A5}$$

$$x_i = x_f + (x_l - x_f)(1 - \cos\theta_i)/2,$$

$$\theta_i = i\pi/N_2,\ i = 1,\ldots,N_2 \tag{A6}$$

on the flap. The ξ coordinate is measured through the control point of each vortex strip. The y coordinate of the control point y_i of each strip is determined by the semicircle

method,[15] as is the strip width distribution. The vector quantity M in Eq. (A1) is defined by

$$M=\frac{a\times\ell}{|a'\times\ell'|^2}\left\{\frac{b'\cdot\ell}{|b'|}-\frac{a'\cdot\ell'}{|a'|}\right\} \tag{A7}$$

where

$$a=(x_{1k}-x_i)i+(y_{1k}-y_i)j+(z_{1k}-z_i)k \tag{A8}$$

$$b=(x_{2k}-x_i)i+(y_{2k}-y_i)j+(z_{2k}-z_i)k \tag{A9}$$

$$a'=(x_{1k}-x_i)i+\beta(y_{1k}-y_i)j+\beta(z_{1k}-z_i)k \tag{A10}$$

$$b'=(x_{2k}-x_i)i+\beta(y_{2k}-y_i)j+\beta(z_{2k}-z_i)k \tag{A11}$$

$$\ell=(x_{2k}-x_{1k})i+(y_{2k}-y_{1k})j+(z_{2k}-z_{1k})k \tag{A12}$$

$$\ell'=(x_{2k}-x_{1k})i+\beta(y_{2k}-y_{1k})j+\beta(z_{2k}-x_{1k})k \tag{A13}$$

and x_{1k}, x_{2k} are computed in a similar manner as given by Eqs. (A3) or (A5), except that they are measured along side edges, not through the control point, of the strip. Therefore, x_i, x_f, and x_t are all for the appropriate side edges. The subscript I denotes the inboard side edge.

Similarly, the induced velocity vector, v_2, due to the associated trailing vortices of the same strip can be shown to be

$$v_2(R_i)\cong\frac{\beta^2}{4\pi}\left[\frac{x_f-x_i}{2}\frac{\pi}{N_I}\sum_{k=I}^{N_I}\gamma(\theta_k)G(\theta_k,R_i)\sin\theta_k+\frac{x_t-x_f}{2}\frac{\pi}{N_2}\sum_{k=I}^{N_2}\gamma(\theta_k)G(\theta_k,R_i)\sin\theta_k\right] \tag{A14}$$

where, for the trailing vortices lying on the xy plane,

$$G=j\frac{z_{2k}-z_i}{\beta^2[(y_i-y_{2k})^2+(z_i-z_{2k})^2]}\left[1-\frac{x_{2k}-x_i}{|b'|}\right]$$

$$-j\frac{z_{1k}-z_i}{\beta^2[(y_i-y_{1k})^2+(z_i-z_{1k})^2]}\left[1-\frac{x_{1k}-x_i}{|a'|}\right]$$

$$-k\frac{y_{2k}-y_i}{\beta^2[(y_i-y_{2k})^2+(z_i-z_{2k})^2]}\left[1-\frac{x_{2k}-x_i}{|b'|}\right]$$

$$+k\frac{y_{1k}-y_i}{\beta^2[(y_i-y_{ik})^2+(z_i-z_{1k})^2]}\left[1-\frac{x_{1k}-x_i}{|a'|}\right] \tag{A15}$$

Adding Eqs. (A1) and (A14), the total induced velocity vector can be obtained. Thus, the normal velocity induced at control point i due to a unit vortex density at k, or the (i,k) element of the influence coefficient matrix $[N]$ can be written as

$$N_{ik}=(\beta^2c_k/8N_k)\sin\theta_k[M(\theta_k,R_i)\cdot n_i+G(\theta_k,R_i)\cdot n_i] \tag{A16}$$

where $c_k=x_f-x_i$, and $N_k=N_I$, if γ_k is on the airfoil; and $c_k=x_t-x_f$, and $N_k=N_2$, if γ_k is on the flap. On the upper and lower jet surfaces and the wing surface, $n_i=k$; whereas on the side surfaces of the rectangular jet, $n_i=\pm j$. Similarly, the elements of the tangential velocity influence coefficient matrix $[S]$ can be written as

$$S_{ik}=(\beta^2c_k/8N_k)\sin\Theta_kM(\theta_k,R_i)\cdot i \tag{A17}$$

where the shallow jet assumption has been made, so that $e=i$. The improvement of evaluating S_{ik} has been discussed in the text.

References

[1] Turner, T. R., Davenport, E. E., and Riebe, J. M., "Low-Speed Investigation of Blowing from Nacelles Mounted Inboard and on the Upper Surface of an Aspect-Ratio-7.0 35° Swept Wing with Fuselage and Various Tail Arrangements," NASA Memo 5-1-59L, June 1959.

[2] Phelps, A. E., III, Letko, W., and Henderson, R. L., "Low-Speed Wind-Tunnel Investigation of a Semispan STOL Jet Transport Wing-Body with an Upper-Surface Blown Jet Flap," NASA, TN D-7183, May 1973.

[3] Aoyagi, K., Falarski, M. D., and Koenig, D. G., "Wind Tunnel Investigation of a Large-Scale Upper Surface Blown-Flap Transport Model Having Two Engines," NASA, TM X-62, 296, 1973.

[4] Phelps, A. E., III and Smith, C. C., Jr., "Wind Tunnel Investigation of an Upper Surface Blown Jet-Flap Powered Lift Configuration," NASA, TN D-7399, 1973.

[5] Smith, C. C., Jr., Phelps, A. E., III, and Copeland, W. L., "Wind Tunnel Investigation of a Large-Scale Semispan Model with an Unswept Wing and an Upper-Surface Blown Jet Flap," NASA TN D-7526, Feb., 1974.

[6] Shivers, J. P. and Smith, C. C., Jr., "Preliminary Static Tests of a Simulated Upper-Surface Blown Jet-Flap Configuration Utilizing a Full-Size Turbofan Engine," NASA, TM X-71931, 1974.

[7] Smith, C. C., Jr., and White, L. C., "Pressure Distribution of a Twin-Engine Upper-Surface Blown Jet-Flap Model," NASA TM X-71937, 1974.

[8] Parlett, L. P., "Free-Flight Wind-Tunnel Investigation of a Four-Engine Swept-Wing Upper-Surface Blown Transport Configuration," NASA TM X-71932, 1974.

[9] Johnson, J. L., Jr. and Phelps, A. E., III, "Low-Speed Aerodynamics of the Upper-Surface Blown Jet Flap," SAE Paper 740470, 1974.

[10] Wimpress, J. K., "Upper Surface Blowing Technology as Applied to the YC-14 Airplane," SAE Paper 730916, 1973.

[11] Lopez, M. L. and Shen, C. C., "Recent Developments in Jet Flap Theory and its Application to STOL Aerodynamic Analysis," AIAA Paper 71-578, 1971.

[12] Küchemann, D. and Weber, J., Chap. 10 *Aerodynamics of Propulsion*, McGraw-Hill, N. Y., 1953.

[13] Lan, C. E. and Campbell, J. F., "Theoretical Aerodynamics of Upper-Surface-Blowing Jet-Wing Interaction," NASA TN D-7936, 1975.

[14] Levinsky, E. S. and Schappelle, R. H., "Analysis of Separation Control by Means of Tangential Blowing," *Journal of Aircraft*, Vol. 12, Jan. 1975, pp. 18-26.

[15] Lan, C. E., "A Quasi Vortex-Lattice Method in Thin Wing Theory," *Journal of Aircraft*, Vol. 11, Sept. 1974, pp. 518-527.

[16] Purcell, E. W., "The Vector Method of Solving Simultaneous Linear Equations," *Journal of Mathematics and Physics*, Vol. 32, July-Oct. 1953, pp. 180-183.

[17] Lan, C. E., "An Analytical Investigation of Wing-Jet Interaction," CR-138140, Chap. 6 and Appendix E, NASA, April 1974.

[18] Spence, D. A., "The Lift Coefficient of a Thin, Jet-Flapped Wing," *Proceedings of the Royal Society (London)* Vol. A238, Dec. 1956, pp. 46-68

[19] Williams, J., Butler, S. F. J., and Wood, M. N., "The Aerodynamics of Jet Flaps," Rept. and Memo. 3304, 1963, Aeronautical Research Council, London, England.

[20] Lan, C. E., "Some Characteristics of Airfoil-Jet Interaction with Mach Number Nonuniformity," *Journal of Aircraft*, Vol. 11, Aug. 1974, pp. 491-494.